

Article

Evaluation of Structural and Functional Properties of $\text{La}_{0.6}\text{Sr}_{0.4}\text{MnO}_3$ Perovskite Prepared by the Fast Solution Combustion Approach

Ramón Cobo Rendón ^{1,*}, Christopher Salvo ², Erwin Sepúlveda ¹, Arunachalam Arulraj ^{3,4}, Felipe Sanhueza ¹, José Jiménez Rodríguez ⁵ and Ramalinga Viswanathan Mangalaraja ^{1,4,*}

¹ Advanced Ceramics and Nanotechnology Laboratory, Department of Materials Engineering, Faculty of Engineering, University of Concepcion, Concepcion 4030000, Chile

² Department of Mechanical Engineering, Faculty of Engineering, Universidad del Bío-Bío, Concepción 4030000, Chile

³ Departamento de Física, Facultad de Ciencias Naturales, Universidad de Atacama, Copiapó 1530000, Chile

⁴ Faculty of Engineering and Sciences, Universidad Adolfo Ibáñez, Diagonal las Torres 2640, Peñalolén, Santiago 1030000, Chile

⁵ National Center for Metallurgical Research, Superior Council of Scientific Investigations (CENIM-CSIC), X-ray Laboratory, 28040 Madrid, Spain

* Correspondence: rcobo@udec.cl (R.C.R.); mangal@uai.cl (R.V.M.)

Abstract: A series of $\text{La}_{0.6}\text{Sr}_{0.4}\text{MnO}_3$ (LSM) perovskite was made using the rapid solution combustion method, which was calcined by varying the temperatures. In order to determine how the calcination temperature affected the nanopowders produced and calcined at various temperatures, their microstructural, morphological, compositional, optical, and electrical properties were analyzed using corresponding characterization tools. The XRD results showed the coexistence of the rhombohedral polymorphs R-3c and Pm-3m for the perovskite phase under a calcination temperature of 1400 °C, which were eliminated with increased calcination temperature. The average grain size was found to increase with increasing calcination temperature. The EDS analysis showed better agreement of the stoichiometry with the theoretical composition. The apparent porosity decreased with increasing temperature due to the coalescence of sintering pores. The sample obtained after calcination at 1500 °C showed 10.3% porosity. The hardness also improved with increasing calcination temperature and reached a maximum value of 0.4 GPa, which matched the bulk density. A similar trend was observed in the resistivity studies as a function of temperature, and all the samples exhibited a low resistivity of ~1.4 Ω·cm in the temperature range of 500–600 °C. The optical characterization showed broad absorption at 560–660 nm and bandwidth values between 3.70 and 3.95 eV, according to the applied heat treatment.

Keywords: LSM; fast solution combustion synthesis; microstructure; hardness; resistivity



Citation: Rendón, R.C.; Salvo, C.; Sepúlveda, E.; Arulraj, A.; Sanhueza, F.; Rodríguez, J.J.; Mangalaraja, R.V. Evaluation of Structural and Functional Properties of $\text{La}_{0.6}\text{Sr}_{0.4}\text{MnO}_3$ Perovskite Prepared by the Fast Solution Combustion Approach. *Catalysts* **2022**, *12*, 1636. <https://doi.org/10.3390/catal12121636>

Academic Editor: Jerry J. Wu

Received: 31 October 2022

Accepted: 6 December 2022

Published: 13 December 2022

Publisher's Note: MDPI stays neutral with regard to jurisdictional claims in published maps and institutional affiliations.



Copyright: © 2022 by the authors. Licensee MDPI, Basel, Switzerland. This article is an open access article distributed under the terms and conditions of the Creative Commons Attribution (CC BY) license (<https://creativecommons.org/licenses/by/4.0/>).

1. Introduction

Perovskites are a class of functional ceramic materials that can be broadly characterized by the general formula of ABX_3 , where X denotes a halide (Cl, Br, or I) or an oxygen ion, which can be further subdivided into perovskite halides and/or oxides. Perovskite halides are widely used in optoelectronic devices and in perovskite solar cells due to their great optical absorption, good charge carrier mobilities, and low optical band gap (1.2–1.4 eV) [1]. A perovskite with oxides is generally termed an ABO_3 or A_2BO_4 structure. A larger cation, A, is situated in the center edge of the structure in a perfect cubic crystalline unit cell of perovskite, whereas a smaller cation, B, is situated in the middle of the octahedron. Both cations are bound by the anion O [2]. A cation, which has 12 oxygen atoms for coordination, can be either rare-earth, alkaline, or alkaline-earth. Any transition metal ion from a 3d, 4d, or 5d configuration can be the B cation, which is encircled by

six oxygen atoms in octahedral coordination. While the B cation is in charge of the catalytic activity in the perovskite structure, the A cation plays a crucial function in stabilizing the structure. As indicated above, the ability to modify a perovskite structure's catalytic characteristics through the partial or complete substitution of A and B cations enables a better fit for the required catalytic applications [3,4]. In many fields, including solid oxide fuel and electrolysis cells (SOFCs and SOECs, respectively) [5], solar cells [1,6], ceramic membranes [7,8], heterogeneous catalysis [3,9], photocatalyst [10,11], water splitting [12], magnetic refrigerators [13], biomaterials, and smart drugs [14], this class of material has shown signs of development. Its unique structure and properties include electronic and ionic conductivity, superconductivity, piezoelectricity, magnetic properties, and catalytic activity [15]. Since Libby [16] and Voorhoeve et al. [17] first studied perovskites in the early 1970s, perovskite-type oxides have gained huge attention as viable catalysts for energy conversion and storage applications. Since then, there has been a huge increase in investigations into perovskite as catalysts or catalytic precursors. Furthermore, due to their ability to hold many oxygen vacancies, they are desirable choices for electrodes in SOFC applications.

The microstructure and composition of electrode materials have a big impact on the performance of SOFCs. The materials that can be employed are constrained by high temperature as well as the presence of oxidizing or reducing atmospheres. Perovskite-oxides can function as catalysts in oxidation and reduction processes, which largely rely on the band structure and the density of states [18]. At the moment, the highest-performing SOFC in the commercial sector is primarily composed of oxygen ion conductors made up of perovskite oxides such as $\text{La}_{0.6}\text{Sr}_{0.4}\text{Co}_{0.2}\text{Fe}_{0.8}\text{O}_3$ (LSCF) or $\text{La}_{0.6}\text{Sr}_{0.4}\text{Co}_{0.2}\text{Fe}_{0.8}\text{O}_3$ (LSM) and $\text{Y}_2\text{O}_3\text{-ZrO}_2$ (YSZ), etc., as a composite cathode [19–23]. These cathode materials exhibit polarization, which is the primary cause of energy loss and low operational stability in SOFCs [24]. Moreover, the high cost of SOFCs is mostly a result of the high production cost of LSM [25]. As a result, one of the major areas of research in SOFCs is synthesizing approaches to these perovskite oxide materials in order to offset their many disadvantages [26], which include cost as well as structural, morphological, electrical, thermal, magnetic, and other issues.

In the current generation of SOFCs, a nominal composition of $\text{La}_{1-x}\text{Sr}_x\text{MnO}_3$ ($x = 0.2$) is typically utilized. Massive magneto-resistance materials are another use for compounds from the doped lanthanum manganite group [27,28]. The use of materials falling under this category is influenced by their final microstructure, grain size, pore size, and pore size distribution, in addition to their chemical, structural, and thermodynamic properties [29–31]. The pore size distribution is crucial for both the permeability of oxygen gas and the conversion of oxygen into oxygen ions, especially in SOFC devices with tubular designs where LSM serves as both a cathode and a support tube. In order to predict the reaction result when the electrolyte interacts with the La–Mn–Zr–O system, the homogeneity of the LSM must also be investigated [31]. In the traditional ceramic synthesis process, which is based on the diffusion of components in their solid state at high temperatures, these features depend on the processing parameters but are hardly adjustable. Hence, the creation of novel, quick, and affordable synthesis methods for usage on a commercial scale, together with the application of tools to assess the effectiveness of processing, is of utmost importance for enhancing the electrode performance in SOFCs and their catalytic activity in energy applications.

Due to its simplicity, cost-effectiveness, and high-quality end product, solution combustion synthesis, which has been used to prepare a variety of compounds for technological applications, particularly in the development of ReSOFC components with the desired composition and structure, is a good option in this situation [32–35]. Thus, in this investigation, we sought to obtain a perovskite-oxides-structured $\text{La}_{0.6}\text{Sr}_{0.4}\text{MnO}_3$ material using the fast combustion synthesis method by dissolving metal nitrates in an aqueous solution and then directly combusting in a single step for only 10 min, obtaining a powder foam that was ground in an agate mortar and subsequently calcined at temperatures of 1400,

1450, or 1500 °C for 8 h. The prepared LSM ($\text{La}_{0.6}\text{Sr}_{0.4}\text{MnO}_3$) perovskite materials' phase formation, shape, crystalline structure, stabilization, electrical, and optical characteristics were thoroughly examined.

2. Results and Discussion

Figure 1 shows the XRD patterns of $\text{La}_{0.6}\text{Sr}_{0.4}\text{MnO}_3$ combusted (LSM500) and calcined at 1400, 1450, and 1500 °C (LSM1400, LSM1450, and LSM1450, respectively). The LSM500 pattern exhibited multiple peaks due to the impurities present in the sample, which were not observed in the calcined samples. Moreover, we noticed an increase in the intensity of the diffraction peaks of the samples calcined at 1450 and 1500 °C and narrowed peaks; this was related to the higher crystallinity [36]. Similarly, the samples LSM1400, LSM1450, and LSM1500 exhibited peaks similar to those in earlier reports [37–39] for a single phase, which corresponds to the single-phase perovskite $\text{La}_{0.6}\text{Sr}_{0.4}\text{MnO}_3$ hexagonal R-3c (JCPDS No.: 98-009-9555). Previous experience has shown the existence of polymorphs with identical nominal compositions during the formation of the LSM phase with this synthesis method [40,41]. In order to study the structural properties of the samples in detail, Rietveld refinements were performed using TOPAS software (Bruker AXS) with the double Voigt function [42].

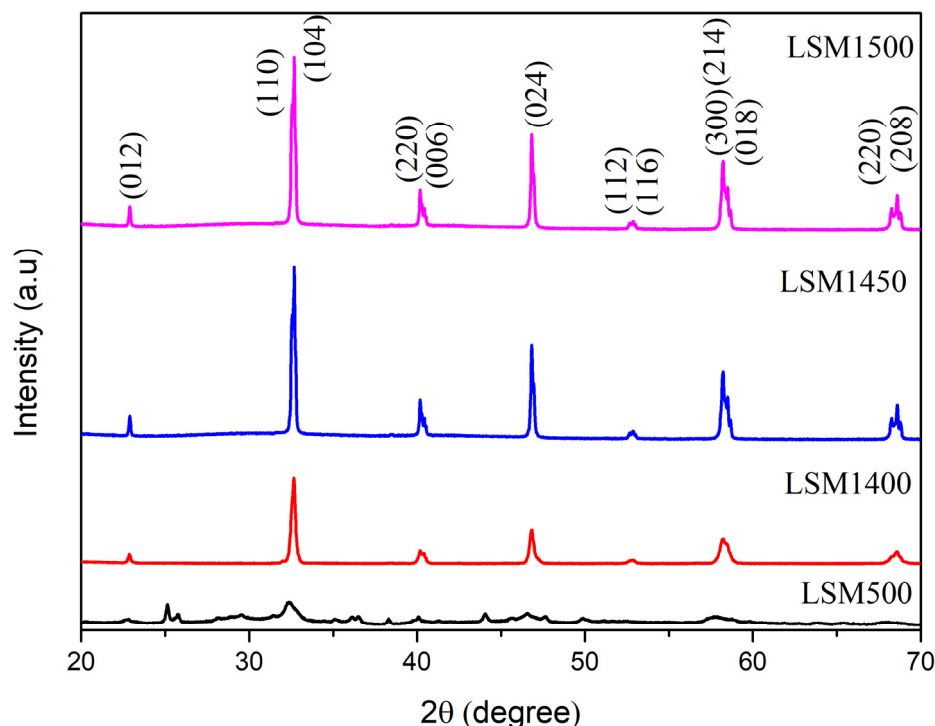


Figure 1. XRD patterns of $\text{La}_{0.6}\text{Sr}_{0.4}\text{MnO}_3$ combusted and calcined at 1400, 1450, and 1500 °C for 8 h.

For sample LSM 1400, the XRD data were modeled with the R-3c space group symmetry as the main perovskite phase. The Pm-3m polymorph was included as the second phase in the refinement; this significantly improved the fit (goodness of fit (GoF)). The difference between the experimental data and the fitted simulated pattern is provided as a continuum. Figure S1 of the supplementary material shows the gray line as the best fit suggesting the coexistence of two distinct polymorphs of $\text{La}_{0.6}\text{Sr}_{0.4}\text{MnO}_3$ in the sample LSM1400 presenting the space group, 96.29% of R-3c and 3.71% of Pm-3m phases. This is likely because LaMnO_3 perovskites adopt a highly symmetric Pm-3m cubic structure at elevated temperatures [42,43]. Islam et al. explained that these ABO_3 -type perovskites can deviate from the ideal cubic structure due to distortions in the rigid BO_6 octahedra, i.e., by changes in the lengths of the B–O bonds, generating flexibility in the antisymmetric Jahn–Teller-type distortion of the BO_6 octahedra [44]. Thus, as the temperature decreases, the

MO₆ octahedron sharing the corners in this structure can tilt, giving rise to the polymorphic transition to the lower symmetry. These distortions are induced by valence bonding, orbital degenerations, polar distortions, valence fluctuations, etc. Therefore, the heat treatment applied to the samples is a crucial factor in influencing the phase segregation. This was further evidenced in the samples LSM1450 and LSM1500, which exhibited a successful fit with a single uniform R-3c phase. The LSM1500 powder showed an improvement in the GoF from the LSM1450 sample, displaying a variation in lattice parameters with the temperature, in an agreement with the literature [38,41,43,44]. The phase quantification and the microstructural parameters of the Rietveld refinement are shown in Table 1.

Table 1. Quantitative analysis of phases and microstructural parameters obtained using Rietveld refinement of LSM samples.

Samples	Phases	Weight %	Lattice Parameters (Å)	O (18e)-Position (x)	Crystallite Size (nm)	R-Factors
LSM1400	La _{0.6} Sr _{0.4} MnO ₃ S.G: R-3c	96.29%	a = b = 5.487 (2) c = 13.352 (3)	0.4516 (1)	>150	R _{exp} = 5.51 R _{wp} = 9.13
	S.G: Pm-3m	3.71%	a = 3.873 (1)		>150	GoF = 1.66
LSM1450	La _{0.6} Sr _{0.4} MnO ₃ S.G: R-3c	100%	a = b = 5.486 (2) c = 13.354 (3)	0.4665 (1)	>150	R _{exp} = 2.61 R _{wp} = 4.41 GoF = 1.69
LSM1500	La _{0.6} Sr _{0.4} MnO ₃ S.G: R-3c	100%	a = b = 5.484 (2) c = 13.346 (3)	0.4686 (1)	>150	R _{exp} = 2.90 R _{wp} = 4.39 GoF = 1.51

Additionally, through this analysis, it was possible to identify the nonexistence of the SrO phase, because it is an undesirable phenomenon highlighted in the literature for perovskites [45–48], as it can lead to a lower electronic conductivity. Squizzato et al. [48] explained that the transition metal B-site of perovskites plays a fundamental role in the catalytic activity, so it is necessary to preserve the pure LSM structure to optimize its oxygen reduction properties in the ReSOFC. With the absence of the SrO phase in all the materials developed by the fast combustion method, it is evident that this synthesis route, and particularly the LSM1500 material, offers a promising crystalline arrangement to use as a catalytic material in the SOFC.

It is well known that the catalytic properties of a material are closely related to the morphology of its particles [49,50]. The morphological effect plays a fundamental role in the performance of the SOFC constituent materials, and the existence of different morphologies may play an important role in influencing the performance of catalysts in particular perovskites. Because of this, the morphology of the synthesized and calcined powders was observed by scanning electron microscopy (SEM), and the images are shown in Figure 2. In LSM500 (Figure 2A), the lack of ordering of its structure is reflected in the SEM because it does not exhibit grain boundaries, which involves the nonformation of defined grains. However, the effect of calcination brings, as a morphological consequence, evidence of clear grain boundaries, an increase in grain size, and a decrease in porosity, as corroborated in Figure 2B–D. As the calcination temperature increases, the grain size distribution significantly increases to exhibit agglomerates up to 3000 nm in sample LSM1500.

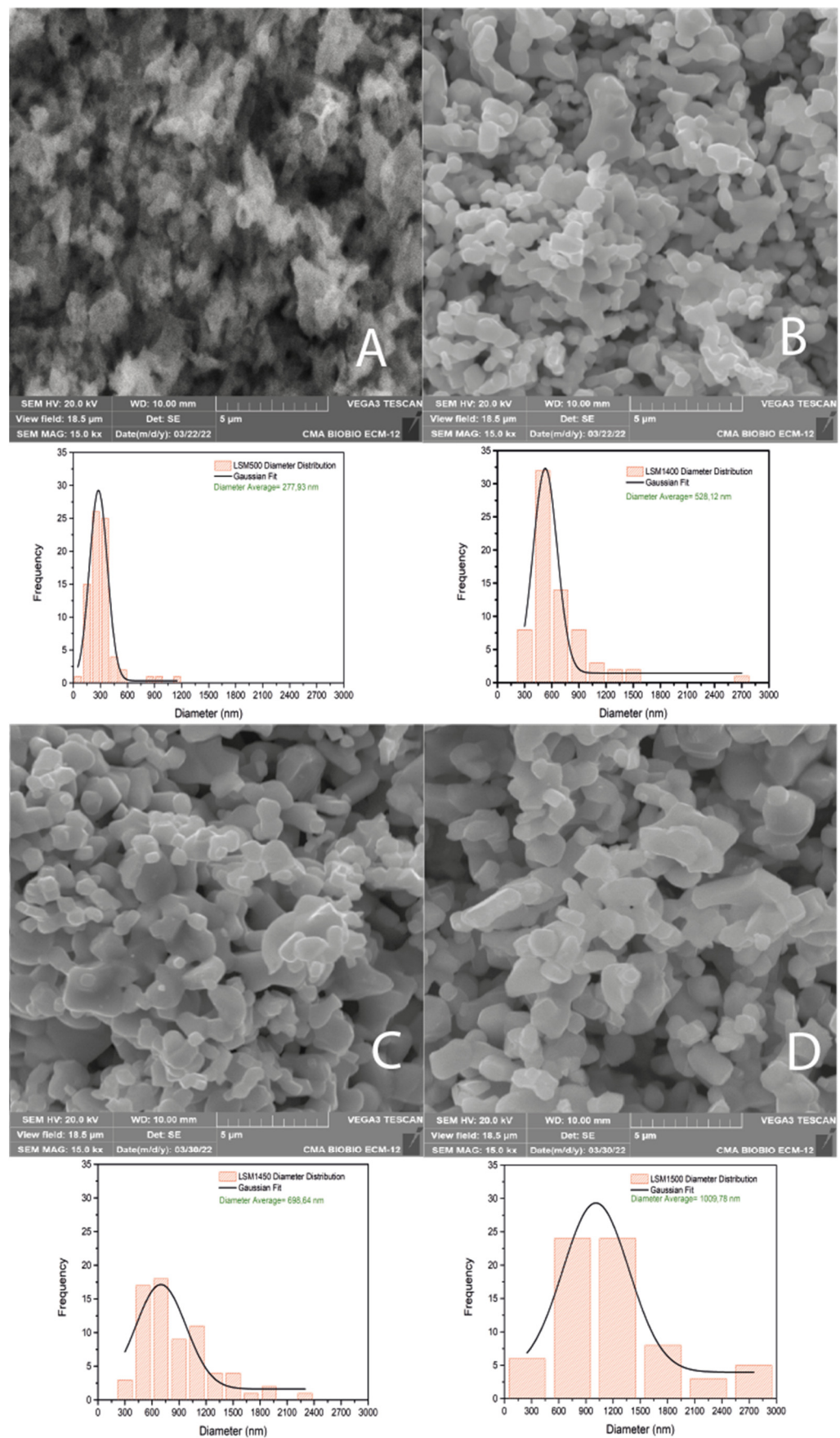


Figure 2. SEM images and corresponding grain size distribution of the combusted and calcined LSM powders: (A) LSM500, (B) LSM1400, (C) LSM1450, and (D) LSM1500.

The prepared sample evidenced a more regular grain size distribution than the previously reported material with a different chemical composition. The regularity of the particles would result in improvements in the catalytic activity due to the ease of charge transfer due to the generation of pores with more homogeneous sizes and volumes [48,50]. The average grain sizes agree with the those in the literature for the synthesized perovskite composition [38,39,51]. Additionally, these SEM images revealed that these grains consisted of La, Sr, Mn, and O in stoichiometric percentage by weight (Table 2). The comparison between theoretical and experimental values of the prepared samples analyzed by EDS exhibited a reasonable stoichiometric control in the synthesis process of the materials (Supplementary Material Figure S2). The effect of calcination in the optimization of the desired stoichiometry was corroborated, because the increase in the calcination temperature led to the differences between the theoretical and experimental values, which were considerably reduced [40,41].

Table 2. Stoichiometric percentage by weight of $\text{La}_{0.6}\text{Sr}_{0.4}\text{MnO}_3$ powder samples calcined at different temperatures.

Samples	Atom	La	Sr	Mn	O
	Stoichiometric	0.6	0.4	1	3
LSM1400	Wt. % (Expe.)	38.59	15.04	24.86	21.51
	Wt. % (Theo.)	37.66	15.84	24.82	21.68
	Difference (%)	2.47	5.05	0.16	0.78
LSM1450	Wt. % (Expe.)	35.45	15.05	24.17	25.33
	Wt. % (Theo.)	37.66	15.84	24.82	21.68
	Difference (%)	5.87	4.99	2.62	16.84
LSM1500	Wt. % (Expe.)	38.33	15.44	24.34	21.89
	Wt. % (Theo.)	37.66	15.84	24.82	21.68
	Difference (%)	1.78	2.53	1.93	0.97

Table 3 shows the apparent density and porosity compared with the grain size and microhardness of the samples. The measurement by the Archimedes method ratified this, which is observed in the SEM and EDS, showing that as the temperature increased, the porosity decreased. The grain size became more prominent, the material was denser, and the microhardness increased up to 0.4 GPa for LSM1500.

Table 3. Mechanical and physical properties of $\text{La}_{0.6}\text{Sr}_{0.4}\text{MnO}_3$ samples obtained at different calcination temperatures.

Sample	LSM1400	LSM1450	LSM1500
Hardness (GPa)	0.2 ± 0.1	0.3 ± 0.1	0.4 ± 0.1
Bulk density (g/cm^3)	6.20	4.58	4.75
Apparent porosity (%)	3.9	21.9	10.3
Average grain size (nm)	528	696	1010

The resistivity variation as a function of temperature is shown in Figure 3. The measurement was performed using the four collinear probes technique, with a DC voltage ranging from -3 to 3 mV with a step of 2×10^{-6} , measuring the current obtained and obtaining the point-to-point resistivity according to Ohm's law. All the evaluated samples exhibited a rapid decrease in resistivity with an increase in temperature, which is typical of LSM samples [52,53], associated with the increased mobility of charge carriers due to electron hopping from Mn^{3+} to Mn^{2+} .

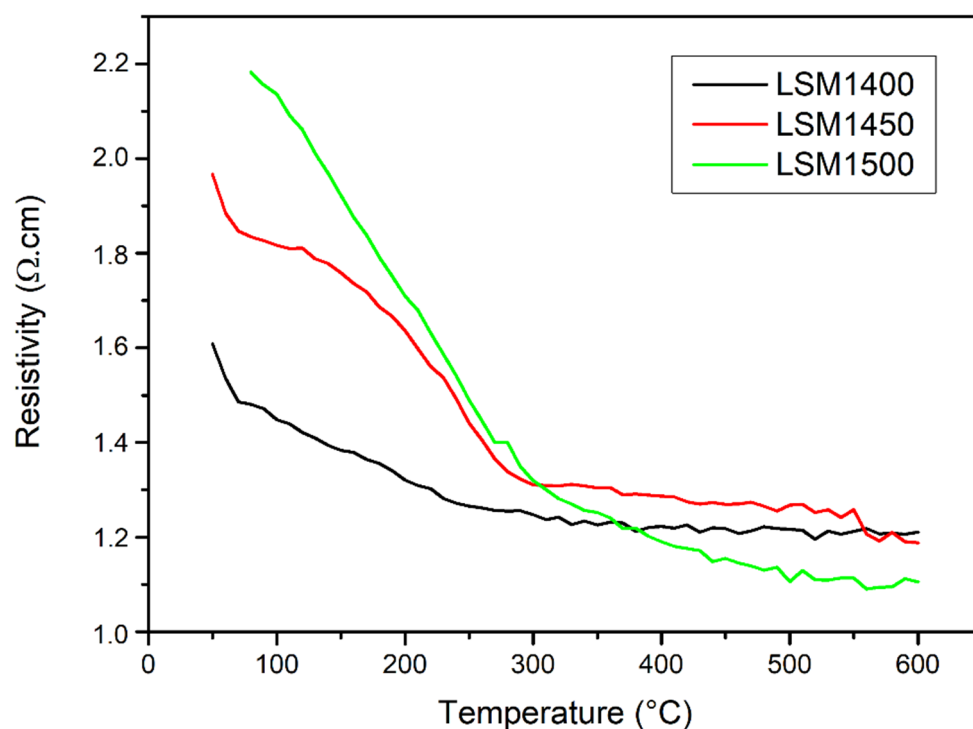


Figure 3. Variation in resistivity with the temperature of the calcined $\text{La}_{0.6}\text{Sr}_{0.4}\text{MnO}_3$ samples.

The effect of calcination was also visible, as the LSM1500 sample presented the steepest resistivity decay gradient compared with the samples calcined at a lower temperature (1400 and 1500°), with a lower resistivity of 1.1 $\Omega\cdot\text{cm}$ at a temperature of 550 °C. This is associated with the intimate relationship between the resistivity and grain size for the LSM samples [41,52–55]. Additionally, there was no difference observed between the samples synthesized using the fast solution combustion approach.

The optical absorption of the samples and the band gap energy (E_g) were evaluated using Wood–Tauc theory [56,57] represented in Figure 4. The optical response of $\text{La}_{0.6}\text{Sr}_{0.4}\text{MnO}_3$ was clearly shown in the wavelength range from 500 to 800 nm, which closely agrees with other investigations [58], with a second absorbance range from 460 nm to 480 nm.

$$(\alpha h\nu)^2 = A(h\nu - E_g) \quad (1)$$

The sample calcined at 1500 °C (LSM1500) showed a better optical response than those calcined at lower temperatures (1400 and 1450 °C), possibly due to its better crystalline and morphological arrangement [41,56,57,59]. The relationship between the band gap energy and the absorption coefficient according to Wood–Tauc theory is formulated by Equation (1), where α is the absorption coefficient; $h\nu$ is the photon energy; and A is a constant that depends on the effective electron mass, hole, and refractive index of the material. The calculated band gap values ranged from 3.71 to 3.95 eV, which are close to the existing reported values for these perovskite materials [57,60–62]. However, the change in the band-gap energy is attributed to the difference in the Mn^{4+} to Mn^{3+} ratio as a function of the La/Sr ratio and the calcination process. Because Sr^{3+} substituted La^{2+} , the thermal treatment led to a product out of stoichiometry; hence, Mn^{3+} must be oxidized to Mn^{4+} to maintain charge neutrality. It is important to point out that these band gap values deepen the versatility of LSM material synthesized this way. In addition to being a good catalyst for the SOFC or ReSOFC, it could be a suitable candidate for photocatalysis processes or for developing high-frequency optoelectronic devices, because the band gap values of the materials are obtained above 2 eV and at absorption values from 500 to 700 nm [10,11,57,63,64].

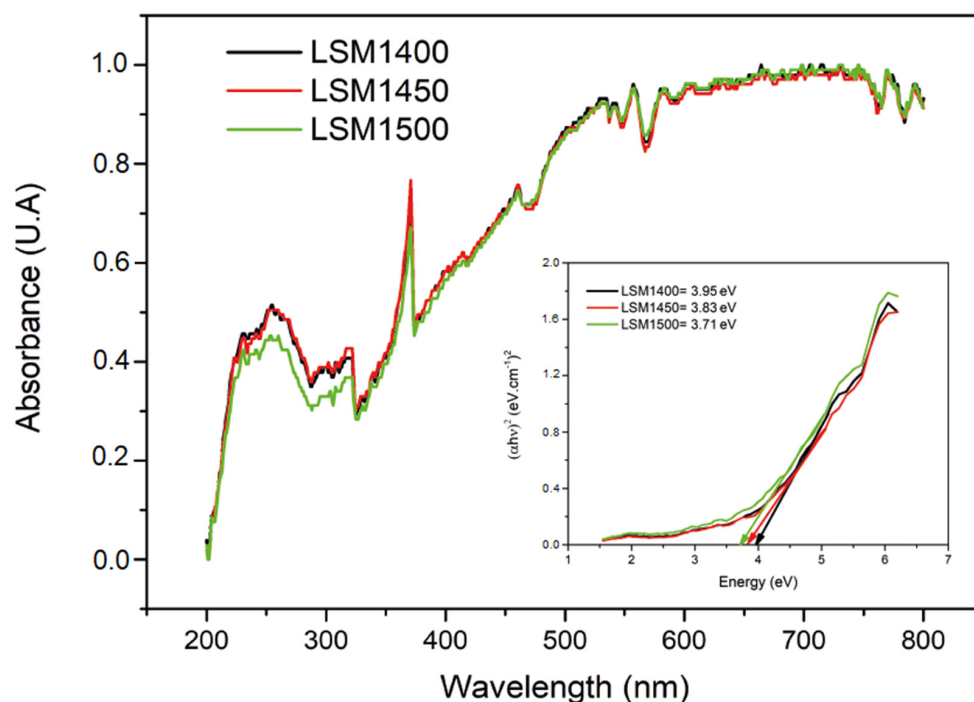


Figure 4. Optical absorbance and band gap spectra of the $\text{La}_{0.6}\text{Sr}_{0.4}\text{MnO}_3$ samples calcined at different temperatures (1400, 1450, or 1500 °C).

3. Materials and Methods

The development of the synthesis of $\text{La}_{0.6}\text{Sr}_{0.4}\text{MnO}_3$ by the fast solution combustion method started with the use of citric acid ($\text{C}_6\text{H}_8\text{O}_7$, 99.99%, Sigma-Aldrich, San Luis, MO, USA) as a fuel in the desired stoichiometric ratio of $\text{La}(\text{NO}_3)_3 \cdot 6\text{H}_2\text{O}$ (99.9%, Merck, Darmstadt, Germany), $\text{Sr}(\text{NO}_3)_2$ (99.8%, Sigma-Aldrich, San Luis, MO, USA), and $\text{Mn}(\text{NO}_3)_2 \cdot 4\text{H}_2\text{O}$ (97%, Sigma-Aldrich, San Luis, MO, USA) as precursors (Table 4). These materials were mixed in 50 mL of water and stirred at room temperature for 1 h. Then, the solution was combusted at 500 °C for 10 min in a Nabertherm furnace, LT 40/12 (Lilienthal, Germany), generating rapid combustion. Finally, the foamed powder was ground in an agate mortar and calcined at different temperatures of 1400, 1450, or 1500 °C for 8 h.

Table 4. Preparation parameters of $\text{La}_{0.6}\text{Sr}_{0.4}\text{MnO}_3$.

Precursors	Grams (g)
$\text{La}(\text{NO}_3)_3 \cdot 6\text{H}_2\text{O}$	2.992
$\text{Sr}(\text{NO}_3)_2$	0.366
$\text{Mn}(\text{NO}_3)_2 \cdot 4\text{H}_2\text{O}$	2.168
$\text{C}_6\text{H}_8\text{O}_7$	2.212

Additionally, 11.5 mm diameter and 1 mm thick pellets were made from the combusted powder by compacting them at 4500 Kg for 1 min. Finally, the pellets were sintered at the same temperatures of 1400, 1450, or 1500 °C. The coding of the samples is provided in Table 5.

The crystal structure and phase of the elements present in the calcined $\text{La}_{0.6}\text{Sr}_{0.4}\text{MnO}_3$ powders were obtained with a X-ray diffractometer (Bruker AXS, D4 Endeavor, Bremen, DE) with 40 kV, 20 mA, and 0.1542 nm Cu- $\text{K}\alpha$ with an angular range of 2θ from 20° to 70° in 0.02° and 1 s steps. In addition, a Rietveld analysis of XRD patterns was carried out to obtain the microstructural information using TOPAS software (Bruker AXS) version 4.2. The morphology, structure, and composition of the material were observed using a

scanning electron microscope (SEM) (Tescan, Vega 3 Easyprobe SBU, Brno, Czech Republic) equipped with an energy-dispersive X-ray detector (EDS). Additionally, the bulk density and porosity were measured using the Archimedes method. The optical property of the materials was measured with a UV–Vis spectrophotometer (Shimadzu UV-2600, Kyoto Japan). The resistivity as a function of temperature (50–700 °C) was examined using the conventional four-collinear probe method with a Keithley 4200-SCS (Cleveland, OH, USA). In addition, the room-temperature mechanical microhardness of the materials was evaluated using a Zwick/Roell 8187.5 ZHU (Santiago, Chile) microhardness tester.

Table 5. La_{0.6}Sr_{0.4}MnO₃ sample nomenclature and parameters.

Temperature (°C)	Time (min/h)	Code Name
500	5 min	LSM500
1400	8 h	LSM1400
1450	8 h	LSM1450
1500	8 h	LSM1500

4. Conclusions

The synthesis of rapid solution combustion was proven as an alternative way to obtain the perovskite compound La_{0.6}Sr_{0.4}MnO₃ through thermal treatment at 1400, 1450, or 1500 °C for 8 h. The results obtained by the XRD indicated that all the samples presented the hexagonal primary crystalline structure (R-3c). The single-phase sample with the best crystalline arrangement was found in LSM1500, with crystallite size >150 nm. The sample LSM1400, analyzed through Rietveld’s analysis of the XRD data, showed the coexistence of R-3c and Pm-3m phases, corroborating the description provided for other compositions with the same synthesis method. The SEM images showed the influence of the heat treatment applied to the samples because there was a close relationship between calcination temperature, grain size, and agglomerate formation. The average grain size for sample LSM1500 was 1010 nm, and agglomerate formation was up to 3 µm. As expected, the porosity decreased with increased calcination temperature, and the hardness reached a maximum value of 0.39 GPa. The EDS analysis showed a close relationship between the heat treatment applied and the stoichiometry optimization. The dependence of resistivity on temperature for the LSM samples showed a decrease in resistivity with an increase in temperature, reaching a resistivity of approximately 1.1 Ω·cm for the sample calcined at 1500 °C, which may be a suitable electrode material for ReSOFCs. Furthermore, the optical response of the fabricated samples occurs in the wavelength range from 500 to 800 nm, and the calculated band gap values ranged from 3.71 to 3.95 eV, which proved that the synthesized perovskite compound may be a suitable candidate for the development of high-frequency optoelectronic devices.

Supplementary Materials: The following supporting information can be downloaded at: <https://www.mdpi.com/article/10.3390/catal12121636/s1>, Figure S1: Rietveld refinement of XRD patterns of La_{0.6}Sr_{0.4}MnO₃ by considering (a) only the rhombohedral R-3c and (b) also the cubic Pm-3m polymorphs of the La_{0.6}Sr_{0.4}MnO₃ perovskite. The difference between experimental data and the fitted simulated pattern is plotted as a continuous gray line at the bottom. (Blue open circles: Experimental data; Green solid line: Cubic phase; Orange solid line: Rhombohedral phase; Red solid line: Fitted data); Figure S2: EDS Mapping of the combusted and calcined LSM powders (A) LSM500, (B) LSM1400, (C) LSM1450, (D) LSM1500.

Author Contributions: Conceptualization, R.V.M. and R.C.R.; methodology, R.C.R.; software, R.C.R., J.J.R., E.S. and C.S.; formal analysis, R.C.R., J.J.R. and C.S.; investigation, R.C.R.; resources, R.V.M., F.S. and J.J.R.; writing—original draft preparation, R.C.R., R.V.M., C.S. and A.A.; writing—review and editing, R.C.R., R.V.M., C.S. and A.A.; visualization, R.C.R. and J.J.R.; supervision, R.V.M.; project administration, R.V.M.; funding acquisition, R.V.M. All authors have read and agreed to the published version of the manuscript.

Funding: This research was funded by FONDECYT-ANID (project No. 1181703) for the financial support, University of Concepcion, Concepcion, Chile.

Data Availability Statement: Data is available on request from the corresponding authors. The data are not publicly available due to the possible extension of the carried work.

Acknowledgments: The author Ramón Cobo-Rendón is grateful to ANID-Chile Grant N°: 21210463, University of Concepcion, Concepcion, Chile.

Conflicts of Interest: The authors declare no conflict of interest.

References

1. Pitaro, M.; Tekelenburg, E.K.; Shao, S.; Loi, M.A. Tin halide perovskites: From fundamental properties to solar cells. *Adv. Mater.* **2022**, *34*, 2105844. [[CrossRef](#)] [[PubMed](#)]
2. Zhu, H.; Zhang, P.; Dai, S. Recent Advances of Lanthanum-Based Perovskite Oxides for Catalysis. *ACS Catal.* **2015**, *5*, 6370–6385. [[CrossRef](#)]
3. Zhu, J.; Li, H.; Zhong, L.; Xiao, P.; Xu, X.; Yang, X.; Zhao, Z.; Li, J. Perovskite Oxides: Preparation, Characterizations, and Applications in Heterogeneous Catalysis. *ACS Catal.* **2014**, *4*, 2917–2940. [[CrossRef](#)]
4. Royer, S.; Duprez, D.; Can, F.; Courtois, X.; Batiot-Dupeyrat, C.; Laassiri, S.; Alamdari, H. Perovskites as Substitutes of Noble Metals for Heterogeneous Catalysis: Dream or Reality. *Chem. Rev.* **2014**, *114*, 10292–10368. [[CrossRef](#)]
5. Hussain, S.; Yangping, L. Review of solid oxide fuel cell materials: Cathode, anode, and electrolyte. *Energy Transit.* **2020**, *4*, 113–126. [[CrossRef](#)]
6. Su, C.; Wang, W.; Shao, Z. Cation-Deficient Perovskites for Clean Energy Conversion. *Accounts Mater. Res.* **2021**, *2*, 477–488. [[CrossRef](#)]
7. Athayde, D.D.; Souza, D.F.; Silva, A.M.; Vasconcelos, D.; Nunes, E.H.; da Costa, J.C.; Vasconcelos, W.L. Review of perovskite ceramic synthesis and membrane preparation methods. *Ceram. Int.* **2016**, *42*, 6555–6571. [[CrossRef](#)]
8. Wang, Z.; Li, Z.; Cui, Y.; Chen, T.; Hu, J.; Kawi, S. Highly efficient NO decomposition via dual-functional catalytic perovskite hollow fiber membrane reactor coupled with partial oxidation of methane at medium-low temperature. *Environ. Sci. Technol.* **2019**, *53*, 9937–9946. [[CrossRef](#)]
9. Hwang, J.; Rao, R.R.; Giordano, L.; Katayama, Y.; Yu, Y.; Shao-Horn, Y. Perovskites in catalysis and electrocatalysis. *Science* **2017**, *358*, 751–756. [[CrossRef](#)]
10. Xu, Y.F.; Yang, M.Z.; Chen, B.X.; Wang, X.D.; Chen, H.Y.; Kuang, D.B.; Su, C.Y. A CsPbBr₃ Perovskite Quantum Dot/Graphene Oxide Composite for Photocatalytic CO₂ Reduction. *J. Am. Chem. Soc.* **2017**, *139*, 5660–5663. [[CrossRef](#)]
11. Zhu, Y.; Liu, Y.; Miller, K.A.; Zhu, H.; Egap, E. Lead Halide Perovskite Nanocrystals as Photocatalysts for PET-RAFT Polymerization under Visible and Near-Infrared Irradiation. *ACS Macro Lett.* **2020**, *9*, 725–730. [[CrossRef](#)] [[PubMed](#)]
12. Sun, H.; Dai, J.; Zhou, W.; Shao, Z. Emerging Strategies for Developing High-Performance Perovskite-Based Materials for Electrochemical Water Splitting. *Energy Fuels* **2020**, *34*, 10547–10567. [[CrossRef](#)]
13. Yu, B.F.; Gao, Q.; Zhang, B.; Meng, X.Z.; Chen, Z. Review on research of room temperature magnetic refrigeration. *Int. J. Refrig.* **2003**, *26*, 622–636. [[CrossRef](#)]
14. Biswas, S.; Keshri, S.; Goswami, S.; Isaac, J.; Ganguly, S.; Perov, N. Antibiotic loading and release studies of LSMO nanoparticles embedded in an acrylic polymer. *Phase Transit.* **2016**, *89*, 1203–1212. [[CrossRef](#)]
15. Žužić, A.; Ressler, A.; Macan, J. Perovskite oxides as active materials in novel alternatives to well-known technologies: A review. *Ceram. Int.* **2022**, *48*, 27240–27261. [[CrossRef](#)]
16. Libby, W.F. Promising Catalyst for Auto Exhaust. *Science* **1971**, *171*, 499–500. [[CrossRef](#)] [[PubMed](#)]
17. Voorhoeve, R.J.H.; Remeika, J.P.; Trimble, L.E. Defect Chemistry and Catalysis in Oxidation and Reduction over Perovskite-Type Oxides. *Ann. N. Y. Acad. Sci.* **2006**, *272*, 3–21. [[CrossRef](#)]
18. Hanif, M.B.; Rauf, S.; Motol, M.; Babar, Z.; Li, C.J.; Li, C.X. Recent progress of perovskite-based electrolyte materials for solid oxide fuel cells and performance optimizing strategies for energy storage applications. *Mat. Res. Bull.* **2022**, *146*, 111612. [[CrossRef](#)]
19. Yang, G.; Su, C.; Shi, H.; Zhu, Y.; Song, Y.; Zhou, W.; Shao, Z. Towards reducing operation temperature of solid oxide fuel cells: Our past fifteen years of efforts in cathode development. *Energ. Fuel.* **2020**, *34*, 15169–15194. [[CrossRef](#)]
20. Park, B.-K.; Barnett, S.A. Boosting solid oxide fuel cell performance via electrolyte thickness reduction and cathode infiltration. *J. Mater. Chem. A.* **2020**, *8*, 11626–11631. [[CrossRef](#)]
21. Wang, W.; Mogensen, M. High-performance lanthanum-ferrite based cathode for SOFC. *Solid State Ion.* **2005**, *176*, 457–462. [[CrossRef](#)]
22. Liu, J.; Zhou, M.; Zhang, Y.; Liu, P.; Liu, Z.; Xie, Y.; Cai, W.; Yu, F.; Zhou, Q.; Wang, X.; et al. Electrochemical Oxidation of Carbon at High Temperature: Principles and Applications. *Energy Fuels* **2017**, *32*, 4107–4117. [[CrossRef](#)]
23. Wang, G.; Zhang, Y.; Han, M. Densification of Ce_{0.9}Gd_{0.1}O_{2-δ} interlayer to improve the stability of La_{0.6}Sr_{0.4}Co_{0.2}Fe_{0.8}O_{3-δ}/Ce_{0.9}Gd_{0.1}O_{2-δ} interface and SOFC. *J. Electroanal. Chem.* **2020**, *857*, 113591–113598. [[CrossRef](#)]
24. Sun, C.; Hui, R.; Roller, J. Cathode materials for solid oxide fuel cells: A review. *J. Solid State Electrochem.* **2010**, *14*, 1125–1144. [[CrossRef](#)]

25. Saha, S.; Ghanawat, S.J.; Purohit, R.D. Solution combustion synthesis of nano particle $\text{La}_{0.9}\text{Sr}_{0.1}\text{MnO}_3$ powder by a unique oxidant-fuel combination and its characterization. *J. Mater. Sci.* **2006**, *41*, 1939–1943. [[CrossRef](#)]
26. Tsvetkov, N.; Lu, Q.; Sun, L.; Crumlin, E.J.; Yildiz, B. Improved chemical and electrochemical stability of perovskite oxides with less reducible cations at the surface. *Nat. Mater.* **2016**, *15*, 1010–1016. [[CrossRef](#)]
27. Jin, S.; Tiefel, T.H.; McCormack, M.; Fastneach, R.A.; Ramesh, R.; Clien, L.H. Thousandfold change in resistivity in magnetoresistive La-Ca-Mn-O films. *Science* **1994**, *264*, 413. [[CrossRef](#)]
28. Mahesh, R.; Mahendiran, R.; Raychaudhuri, A.K.; Rao, C.N.R. Effect of particle size on the giant magnetoresistance of $\text{La}_{0.7}\text{Ca}_{0.3}\text{MnO}_3$. *Appl. Phys. Lett.* **1996**, *68*, 2291. [[CrossRef](#)]
29. Huang, Y.H.; Xu, Z.G.; Yan, C.H.; Wang, Z.M.; Zhu, T.; Liao, C.S.; Gao, S.; Xu, G.X. Soft chemical synthesis and transport properties of $\text{La}_{0.7}\text{Sr}_{0.3}\text{MnO}_3$ granular perovskites. *Solid State Commun.* **2000**, *114*, 43. [[CrossRef](#)]
30. Zhang, N.; Ding, W.; Zhong, W.; Xing, D.; Du, Y. Tunnel-type giant magnetoresistance in the granular perovskite $\text{La}_{0.85}\text{Sr}_{0.15}\text{MnO}_3$. *Phys. Rev. B* **1997**, *B56*, 8138. [[CrossRef](#)]
31. Yokokawa, H.; Sakai, N.; Kawada, T.; Dokiwa, M. Thermodynamic analysis on interface between perovskite electrode and YSZ electrolyte. *Solid State Ion.* **1990**, *40*, 398. [[CrossRef](#)]
32. Mangalaraja, R.; Mouzon, J.; Hedström, P.; Camurri, C.P.; Ananthakumar, S.; Odén, M. Microwave assisted combustion synthesis of nanocrystalline yttria and its powder characteristics. *Powder Technol.* **2009**, *191*, 309–314. [[CrossRef](#)]
33. Marinšek, M.; Zupan, K.; Maček, J. Ni-YSZ cermet anodes prepared by citrate/nitrate combustion synthesis. *J. Power Sources* **2002**, *106*, 178–188. [[CrossRef](#)]
34. Wang, W.; Huang, Y.; Jung, S.; Vohs, J.M.; Gorte, R.J. A Comparison of LSM, LSF, and LSCo for Solid Oxide Electrolyzer Anodes. *J. Electrochem. Soc.* **2006**, *153*, A2066–A2070. [[CrossRef](#)]
35. Gan, L.M.; Chan, H.S.; Zhang, L.H.; Chew, C.H.; Loo, B.H. Preparation of fine LaNiO_3 powder from oxalate precursors via reactions in inverse micro emulsions. *Mater. Chem. Phys.* **1994**, *37*, 263–268. [[CrossRef](#)]
36. Di Florio, G.; Macchi, E.G.; Mongibello, L.; Baratto, M.C.; Basosi, R.; Busi, E.; Caliano, M.; Cigolotti, V.; Testi, M.; Trini, M. Comparative life cycle assessment of two different SOFC-based cogeneration systems with thermal energy storage integrated into a single family house nanogrid. *Appl. Energ.* **2021**, *285–304*, 116378–116397. [[CrossRef](#)]
37. Neagu, D.; Irvine, J.T. Structure and properties of $\text{La}_{0.4}\text{Sr}_{0.4}\text{TiO}_3$ ceramics for use as anode materials in solid oxide fuel cells. *Chem. Mater.* **2010**, *22*, 5042–5053. [[CrossRef](#)]
38. Raoufi, T.; Ehsani, M.; Khoshnoud, D.S. Critical behavior near the paramagnetic to ferromagnetic phase transition temperature in $\text{La}_{0.6}\text{Sr}_{0.4}\text{MnO}_3$ ceramic: A comparison between sol-gel and solid state process. *Ceram. Int.* **2017**, *43*, 5204–5215. [[CrossRef](#)]
39. Sanna, C.; Squizzato, E.; Costamagna, P.; Holtappels, P.; Glisenti, A. Electrochemical study of symmetrical intermediate temperature-solid oxide fuel cells based on $\text{La}_{0.6}\text{Sr}_{0.4}\text{MnO}_3/\text{Ce}_{0.9}\text{Gd}_{0.1}\text{O}_{1.95}$ for operation in direct methane/air. *Electrochim. Acta* **2022**, *409*, 139939. [[CrossRef](#)]
40. Durango-Petro, J.; Salvo, C.; Usuba, J.; Abarzua, G.; Sanhueza, F.; Mangalaraja, R.V. Fast Solution Synthesis of NiO-Gd_{0.1}Ce_{0.9}O_{1.95} Nanocomposite via Different Approach: Influence of Processing Parameters and Characterizations. *Materials* **2021**, *14*, 3437. [[CrossRef](#)]
41. Rendón, R.C.; Udayabhaskar, R.; Salvo, C.; Sepúlveda, E.; Rodríguez, J.J.; Camurri, C.P.; Viswanathan, M.R. Evaluation of $\text{La}_{0.8}\text{Sr}_{0.2}\text{MnO}_3$ perovskite prepared by fast solution combustion. *Ceram. Int.* **2022**, *48*, 35100–35107. [[CrossRef](#)]
42. Balzar, D.; Ledbetter, H. Voigt-function modeling in Fourier analysis of size- and strain-broadened X-ray diffraction peaks. *J. Appl. Crystallogr.* **1993**, *26*, 97–103. [[CrossRef](#)]
43. Coey, J.M.D.; Viret, M.; Von Molnár, S. Mixed-valence manganites. *Adv. Phys.* **1999**, *48*, 167–293. [[CrossRef](#)]
44. Islam, M.A.; Rondinelli, J.M.; Spanier, J.E. Normal mode determination of perovskite crystal structures with octahedral rotations: Theory and applications. *J. Phys. Condens. Matter* **2013**, *25*, 175902. [[CrossRef](#)]
45. Wu, Q.-H.; Liu, M.; Jaegermann, W. X-ray photoelectron spectroscopy of $\text{La}_{0.5}\text{Sr}_{0.5}\text{MnO}_3$. *Mater. Lett.* **2005**, *59*, 1980–1983. [[CrossRef](#)]
46. Caillol, N.; Pijolat, M.; Siebert, E. Investigation of chemisorbed oxygen, surface segregation and effect of post-treatments on $\text{La}_{0.8}\text{Sr}_{0.2}\text{MnO}_3$ powder and screen-printed layers for solid oxide fuel cell cathodes. *Appl. Surf. Sci.* **2007**, *253*, 4641–4648. [[CrossRef](#)]
47. Jiang, S. The electrochemical performance of LSM/zirconia-yttria interface as a function of a-site non-stoichiometry and cathodic current treatment. *Solid State Ionics* **1999**, *121*, 1–10. [[CrossRef](#)]
48. Squizzato, E.; Sanna, C.; Glisenti, A.; Costamagna, P. Structural and catalytic characterization of $\text{La}_{0.6}\text{Sr}_{0.4}\text{MnO}_3$ nanofibers for application in direct methane intermediate temperature solid oxide fuel cell anodes. *Energies* **2021**, *14*, 3602. [[CrossRef](#)]
49. Xie, X.; Li, Y.; Liu, Z.-Q.; Haruta, M.; Shen, W. Low-temperature oxidation of CO catalysed by Co_3O_4 nanorods. *Nature* **2009**, *458*, 746–749. [[CrossRef](#)]
50. Arandiyán, H.; Dai, H.; Deng, J.; Liu, Y.; Bai, B.; Wang, Y.; Li, X.; Xie, S.; Li, J. Three-dimensionally ordered macroporous $\text{La}_{0.6}\text{Sr}_{0.4}\text{MnO}_3$ with high surface areas: Active catalysts for the combustion of methane. *J. Catal.* **2013**, *307*, 327–339. [[CrossRef](#)]
51. Huang, F.; Sun, X.; Zheng, Y.; Xiao, Y.; Zheng, Y. Facile co precipitation synthesis of $\text{La}_{0.6}\text{Sr}_{0.4}\text{MnO}_3$ perovskites with high surface area. *Mater. Lett.* **2018**, *210*, 287–290. [[CrossRef](#)]
52. Saleem, M.; Varshney, D. Structural, thermal, and transport properties of $\text{La}_{0.67}\text{Sr}_{0.33}\text{MnO}_3$ nanoparticles synthesized via the sol-gel auto-combustion technique. *RSC Adv.* **2018**, *8*, 1600–1609. [[CrossRef](#)] [[PubMed](#)]

53. Shinde, K.P.; Thorat, N.D.; Pawar, S.S.; Pawar, S.H. Combustion synthesis and characterization of perovskite $\text{La}_{0.9}\text{Sr}_{0.1}\text{MnO}_3$. *Mater. Chem. Phys.* **2012**, *134*, 881–885. [[CrossRef](#)]
54. Varshney, D.; Dodiya, N. Electrical resistivity of the hole doped $\text{La}_{0.8}\text{Sr}_{0.2}\text{MnO}_3$ manganites: Role of electron–electron/phonon/magnon interactions. *Mater. Chem. Phys.* **2011**, *129*, 896–904. [[CrossRef](#)]
55. Zhu, N.; Liu, Y.J. Prediction of the Magneto-Resistance of $\text{La}_{0.65}\text{Ca}_{0.35}\text{MnO}_3$ and $\text{La}_{0.8}\text{Sr}_{0.2}\text{MnO}_3$ via Temperature and Magnetic Field. In *Advanced Materials Research*; Trans Tech Publications Ltd.: Bäch, Switzerland, 2013.
56. Rashad, M.M.; Turkey, A.O.; Kandil, A.T. Optical and electrical properties of $\text{Ba}_{1-x}\text{Sr}_x\text{TiO}_3$ nanopowders at different Sr^{2+} ion content. *J. Mater. Sci. Mater. Electron.* **2013**, *24*, 3284–3291. [[CrossRef](#)]
57. Turkey, A.O.; Rashad, M.M.; Zaki, Z.I.; Ibrahim, I.A.; Bechelany, M. Tuning the optical and dielectric properties of calcium copper titanate $\text{Ca}_x\text{Cu}_{3-x}\text{Ti}_4\text{O}_{12}$ nanopowders. *RSC Adv.* **2015**, *5*, 18767–18772. [[CrossRef](#)]
58. Cui, K.; Cheng, Y.; Dai, J.; Liu, J. Synthesis, characterization and microwave absorption properties of $\text{La}_{0.6}\text{Sr}_{0.4}\text{MnO}_3$ /polyaniline composite. *Mater. Chem. Phys.* **2013**, *138*, 810–816. [[CrossRef](#)]
59. Afje, F.R.; Ehsani, M. Size-dependent photocatalytic activity of $\text{La}_{0.8}\text{Sr}_{0.2}\text{MnO}_3$ nanoparticles prepared by hydrothermal synthesis. *Mater. Res. Express* **2018**, *5*, 045012. [[CrossRef](#)]
60. Cesaria, M.; Caricato, A.P.; Leggieri, G.; Martino, M.; Maruccio, G. Optical response of oxygen deficient $\text{La}_{0.7}\text{Sr}_{0.3}\text{MnO}_3$ thin films deposited by pulsed laser deposition. *Thin Solid Film.* **2013**, *545*, 592–600. [[CrossRef](#)]
61. Busse, P.; Yin, Z.; Mierwaldt, D.; Scholz, J.; Kressdorf, B.; Glaser, L.; Miedema, P.S.; Rothkirch, A.; Viehhaus, J.; Jooss, C.; et al. Probing the surface of $\text{La}_{0.6}\text{Sr}_{0.4}\text{MnO}_3$ in water vapor by in situ photon-in/photon-out spectroscopy. *J. Phys. Chem. C* **2020**, *124*, 7893–7902. [[CrossRef](#)]
62. Liu, X.L.; Machida, A.M.; Moritomo, Y.M.; Ichida, M.I.; Nakamura, A.N. Room-temperature photo switching in $\text{La}_{0.6}\text{Sr}_{0.4}\text{MnO}_3$ film. *Jpn. J. Appl. Phys.* **2000**, *39*, L670. [[CrossRef](#)]
63. de Jong, M.P.; Dediú, V.A.; Taliani, C.; Salaneck, W.R. Electronic structure of $\text{La}_{0.7}\text{Sr}_{0.3}\text{MnO}_3$ thin films for hybrid organic/inorganic spintronics applications. *J. Appl. Phys.* **2003**, *94*, 7292–7296. [[CrossRef](#)]
64. Takenaka, K.; Sawaki, Y.; Shiozaki, R.; Sugai, S. Electronic structure of the double-exchange ferromagnet $\text{La}_{0.825}\text{Sr}_{0.175}\text{MnO}_3$ studied by optical reflectivity. *Phys. Rev. B* **2000**, *62*, 13864. [[CrossRef](#)]